Supplementary Information

Interface rich CuO/Al_2CuO_4 surface for selective ethylene production from electrochemical CO_2 conversion

Siraj Sultan,[†a] HoJeong Lee,[†a] Sojung Park,[†b] Minho M. Kim,[†c] Aram Yoon, [†df] Hansaem Choi,[a] Tae-Hoon Kong,[a] Young-Jin Koe,[e] Hyung-Suk Oh,[e] Zonghoon Lee,*[df] Hyungjun Kim,*[c] Wooyul Kim*[b] and Youngkook Kwon*[a]

[a] School of Energy and Chemical Engineering, Ulsan National University of Science and Technology (UNIST), Ulsan 44919, Republic of Korea.

[b] Department of Energy Engineering / KENTECH Institute for Environmental and Climate Technology, Korea Institute of Energy Technology.

[c] Department of Chemistry, Korea Advanced Institute of Science and Technology (KAIST), Daejeon 34141, Republic of Korea.

[d] Department of Materials Science and Engineering, UNIST, Ulsan 44919, Republic of Korea.

[e] Clean Energy Research Center, Korea Institute of Science and Technology (KIST), Seoul 02792, Republic of Korea

[f] Center for Multidimensional Carbon Materials, Institute for Basic Science (IBS), UNIST, Ulsan 44919, Republic of Korea

*Correspondence and requests for materials should be addressed to Y.K. (ykwon@unist.ac.kr), W.K (wkim@kentech.ac.kr), H.K (linus16@kaist.ac.kr) and Z.L (zhlee@unist.ac.kr).

[†] These authors contributed equally to this work.

Supplementary Methods

Chemicals: Copper (II) nitrate trihydrate ($Cu(NO_3)_2.3H_2O$, 99.99%), aluminium nitrate nonahydrate ($Al(NO_3)_3{\cdot}9H_2O$, 98%), ammonium carbonate ($(NH_4)_2CO_3$, 99.99%), Nafion 117 solution (5 wt% in mixture of lower aliphatic alcohols and water, contains 45% water), 2-propanol ($(CH_3)_2CHOH$, anhydrous 99.5%), NH_4F (≥98.0%; ACS Reagent), Na_2SO_3 (≥98.0%), NH_4Cl (99.998%; trace metals basis), $Na_2S_2O_3$. $5H_2O$ (≥99.5%; ACS Reagent), $NaAuCl_4 \cdot 2H_2O$ (99%), $KHCO_3$ (≥99.95% trace metals basis, 99.7-100.5% dry basis) and D_2O (99.9 atom % D) were purchased from Sigma-Aldrich. Alumina polishing suspensions and alumina pads were purchased from BASi Inc (PK-4 Electrode Polishing Kit). Ultrapure deionized water (DI water, resistivity ≥18.2 MΩ cm) was used in all experiments which was prepared using a Human-Power I+ water purification system (Human Corporation).

Characterization techniques: TEM, HRTEM, HAADF–STEM images and EDS mapping were taken on JEOL JEM-2100F at an acceleration voltage of 200 kV. Samples for TEM analysis were prepared by dropping the colloidal solution of the catalyst (catalyst powder was thoroughly dispersed in anhydrous ethanol) on a carbon-coated nickel grid (Holey carbon-Ni, 200 mesh, 50 micron) and dried overnight at room temperature. To observe the clear crystal structures of CuO and Al_2CuO_4 in CuO/Al_2CuO_4-23, additional HAADF–STEM images, EDS mapping and line-scan analysis were performed using aberration-corrected TEM (FEI Titan3 G2 60-300) at 80 kV. XRD analysis was carried out on a RIGAKU SmartLab in 2Θ range of 10-90° using Cu Kα1 (λ = 0.15406 nm) radiation source. XPS analysis was measured on K-Alpha (Thermo Fisher, UK) instrument. The weight percent of Cu and Al in the synthesized catalysts (CuAl-**1** to CuAl-**3**) were obtained with ICP-OES (700-ES, Varian). XAS data for the Cu K-edge were acquired in transmission mode using beamline 6D of Pohang Accelerator Laboratory (PAL). Background subtraction, normalization, and Fourier-transform were done by standard procedure with the ATHENA program. The extracted XANES, (FT) EXAFS and k3χ (k) oscillation signals of Cu metal were analyzed for all four catalysts.

Ex situ and in situ/operando X-ray absorption analysis: X-ray absorption fine structure spectroscopy (XAFS) data for the Cu K-edge were acquired in transmission mode using the 6D UNIST beamline located at the Pohang Accelerator Laboratory (PAL). The operando XAFS experiments were performed on the 1D KIST beamline located in PAL. The working electrode was prepared by depositing 0.6 mg of CuAl-**1** catalyst on 2.5×1.5 cm^2 Toray carbon paper. The working electrode, reference electrode (Ag/AgCl) and counter electrode (Pt foil) were mounted onto a homemade gas-fed XAFS fluorescence electrochemical cell, adapted for the in-situ experiments. As an electrolyte, we used high purity CO_2 saturated 0.1 M $KHCO_3$ solution and the flow of CO_2 (flow rate: 5 sccm) was maintained during the operando XAFS-electrochemical CO_2RR experiments. The electrochemical experiments for the operando XAFS analysis was carried out under the chronoamperometric conditions, where the electrode was biased at different applied potentials from the open-circuit voltage (OCV) down to -1.05 V, same with the CO_2RR activity measurement condition. The EXAFS spectrum at each potential took about 20 min. The applied potential was controlled through the VSP-modular potentiostat. Background subtraction, normalization, and Fourier-transform were done by standard procedure with the ATHENA program. The extracted XANES, (FT) EXAFS and k3χ (k) oscillation signals of Cu metal were analyzed for all four catalysts.

Flow-cell measurements: For the flow-cell experiment, the electrode for the cathode was prepared by spraying 20 mL of well-mixed catalyst ink containing 50 mg of catalyst, 313 µL of Nafion and 19.687 mL of ethanol onto a 4 cm^2 carbon gas-

diffusion electrode (GDE, Sigracet, Fuel Cell Store). The total catalyst load on the GDE was 0.6 mg cm^{-2} (the GDE after spraying and drying with ink was weighed for the total amount of catalyst on its surface). The GDE with catalyst and Hg/HgO (1 M NaOH) was used as working and reference electrodes in the cathode chamber and the Ni-Fe-Mo foil as a counter electrode in the anode chamber. The cathode and anode chambers were separated by an anion-exchange membrane (AEM, Fumapem FAA-3-PK-130). The cathode area exposed to electrolyte and CO_2 gas was 1 cm^2, while the anode area was 2.0×2.0 cm^2. 1.0 M aqueous KOH solution was used as both catholyte and anolyte. During electrochemical measurements, the electrolyte was circulated into the cathode and anode chambers at a flow rate of 6.0 mL min^{-1} and the CO_2 gas with a flow rate of 20.0 sccm was fed directly into the cathode gas compartment. Note: In a flow-cell electrolyzer, the strong CO_2 capturing ability of the KOH solution and the high conversion rate of CO_2 into gas/liquid products due to high current densities can significantly change the gas outlet flow rate from the reactor to gas chromatography (GC), therefore, the faradaic efficiency (FE) of the gas products can be calculated on the outlet gas flow rate but not the inlet gas flow rate.[1] Thus, to obtain reliable and accurate FE for each gas product, we carefully monitored the outlet gas flow rate from the flow-cell reactor to the GC by a flow meter and use it for the FE calculations. The electrochemical CO_2RR activity in the Flow-cell system was measured by the chronopotentiometry measurements method in the current densities ranges of 100-1000 mA cm^2.

Electrode preparation for Attenuated total reflection-surface enhanced infrared absorption spectroscopy (ATR-SEIRAS) measurement: The catalysts (CuO and CuAl-**1**) ink was prepared by dispersing 1 mg of catalyst powder with 6 µL Nafion solution in 0.6 mL of isopropyl alcohol by ultrasonication. To prepare the electrode, 0.5 mL of ink was sprayed onto the Au coated Si prism electrode with 0.5 cm^2 of an active area using a spray gun. The electrode was dried in air for the subsequent electrochemical tests. Au thin films were prepared by an electroless plating procedure.[2] The reflective plane of a 60° Si prism (Veemax, 2 cm in diameter) was sequentially polished with alumina pastes for 10-15 min each to obtain a fresh Si layer. The crystal was then rinsed in a constant stream of DI water for 5-10 min while wiping it with a wet Kim-wipe. Sequentially, the Si surface was etched by immersing the reflective plane of the prism in an aqueous solution of 40 wt. % NH_4F (25 °C) for 1 min. After etching, the prism was rinsed with DI water and the reflectve surface was immersed in the mixture of the Au plating solution (0.015 M $NaAuCl_4 \bullet 2H_2O$ + 0.15 M Na_2SO_3 + 0.05 M $Na_2S_2O_3 \bullet 5H_2O$ + 0.05 M NH_4Cl and a 2 wt% hydrofluoric acid solution in a 1:2 volume ratio; T = 60 °C) for 2 min, rinsed with DI water and dried. The CuO and CuAl-**1** catalysts were prepared on the Au coated Si prism according to the aforementioned procedure.

In-situ ATR-SEIRAS measurements: The working electrode prepared on Si prism was placed in a two-compartment with a three-electrode Spectro-electrochemical cell. The working electrode (CuO or CuAl-**1**), and the reference electrode (Ag/AgCl: Basi, 3 M NaCl) were separated from the platinum wire (counter electrode) by a selemion AMV anion exchange membrane. The only stirring effect inside the cell was from various bubbled gases. The cell was integrated into the Fourier Transform Infrared Spectrophotometer (VERTEX 80v, Bruker) equipped with a mercury cadmium telluride (MCT) detector and a variable angle specular reflectance accessory (VeemaxⅢ, Pike technologies). The electrochemical measurements for the ATR-SEIRAS were performed on Autolab PGSTAT204 potentiostat. The electrochemical measurements were carried out in 0.1 M $KHCO_3$ D_2O electrolyte at room temperature and the electrode catalysts before the measurements were activated by cyclic

voltammetry from -0.55 to -2.2 V (vs. Ag/AgCl) at a scan rate of 0.02 V s^{-1} in CO_2 saturated electrolyte for a total of three cycles. Before activation, the constant flow of CO_2 gas (19-20 sccm, adjusted by a mass flow controller: MC-100SCCM-D; Alicat Scientific) was purged into the electrolyte for 1 h to form a CO_2 saturated solution and maintain the CO_2 flow throughout the electrochemical experiments. All spectroscopic measurements were conducted with a spectral resolution of 4 cm^{-1}. The spectra were presented in absorbance, with positive and negative peaks showing an increase and decrease in the signal, respectively.

In-situ ATR-SEIRAS measurements during the chronoamperometric scan were carried out with a time resolution of ~60 s. The cathodic chronoamperometric scan was conducted from -0.5 to -2.2 V (vs. Ag/AgCl) with 0.1 V intervals. Each potential was maintained for 2 min and the corresponding IR spectra for each potential were collected simultaneously with the time of applying potential.

Time-resolved IR measurements at a fixed potential were performed with a time resolution of ~3 s. A target potential was applied for 2 min. Spectra acquisition was initiated 60 seconds before applying the desired potential. The spectrum collected at -0.9 V (vs. Ag/AgCl) was used as the baseline.

Faradaic efficiency: Faradaic efficiency (FE) for the CO_2RR products in H-Cell were calculated according to the following equations and procedures. For our FE calculation, we take the example of C_2H_4.

$$FE_{C_2H_4} = \frac{z \cdot \dot{n}_{C_2H_4} \cdot F}{Q/t} \qquad (1)$$

In equation 1, z is the transfer of electrons [for C_2H_4 the z value is 12 $\frac{mol_{e^-}}{mol_{C_2H_4}}$ according to the equation; $2CO_2 + 12H^+ + 12e^- \rightarrow C_2H_4 + 4H_2O$], $\dot{n}_{C_2H_4}$ is the number of mol of C_2H_4 produced per second, which is calculated according to equation 2. F is the Faraday constant (96,485 C mol^{-1}), and Q is the charge in coulomb, which was -3.215 $*10^{-3}$ A.

$$\dot{n}_{C_2H_4} = \frac{P \times v_{C_2H_4}}{R \times T} \qquad (2)$$

In equation 2, P is pressure in the atmosphere (1 atm), $v_{C_2H_4}$ is the volumetric flow rate of C_2H_4 in L/S, R is the gas constant [R= 0.082 L. atm/K. mol and T is the temperature based on our laboratory condition (293 K).

The volumetric flow rate of C_2H_4 was evaluated from the GC flame ionization detector data and the GC calibration data (Fig. S20, ESI) according to equations 3 to 5. In the raw GC flame ionization detector data, the peaks at 2.397, 4.232, 6.245, 10.068 retention times correspond to CO, CH_4, unreacted CO_2, and C_2H_4, respectively (Note: the peak at 11.388 retention time corresponds to C_2H_6, which was an impurity in the reactant CO_2 gas, which was confirmed by GC).

The portion of the C_2H_4 in the outlet gas was calculated from equation 4, which used the relationship between ppm and peak area of C_2H_4 from the GC calibration data in equation 3.

$$\frac{ppm_{C_2H_4}}{Peak\ area_{C_2H_4}} = 4.48535 * 10^{-5} \qquad (3)$$

$$portion_{C_2H_4} = Peak\ area_{C_2H_4} \times 4.48535 * 10^{-5}\ ppm \qquad (4)$$

Thus, the portion of C_2H_4 in the outlet gas was:

$$portion_{C_2H_4} = 17{,}511{,}208 \times 4.48535 * 10^{-5}\ ppm$$

$$portion_{C_2H_4} = 785.439\ ppm$$

$$portion_{C_2H_4} = 0.0785439\ \%$$

The volumetric flow rate of C_2H_4 was calculated according to equation 5.

$$v_{C_2H_4} = v_{total} \times portion_{C_2H_4} \qquad (5)$$

In equation 5, v_{total} is the volumetric flow rate of the outlet gas (4.2 ml min^{-1}).

$$v_{C_2H_4} = 4.2\,\frac{mL}{min} \times 0.0785439\ \%$$

$$v_{C_2H_4} = 3.29884 * 10^{-3}\,\frac{mL}{min}$$

$$v_{C_2H_4} = 5.49807 * 10^{-8}$$

Thus, the number of mol of C_2H_4 produced per second according to equation 2 is:

$$\dot{n}_{C_2H_4} = \frac{1atm \times 5.49807 * 10^{-8}\,\frac{L}{s}}{0.082\frac{L.atm}{K.mol} \times 293K} = 2.28838 * 10^{-9}\,\frac{mol_{C_2H_4}}{s}$$

Finally, the FE of C_2H_4 according to equation 1 is:

$$\mathrm{FE}_{C_2H_4} = \frac{12\,\frac{mol_{e^-}}{mol_{C_2H_4}} \times 2.28838 * 10^{-9} \times 96485\,\frac{C}{mol_{e^-}}}{3.215 * 10^{-3}\,\frac{C}{s}} \times 100[\%] \quad = 82.4\ \%$$

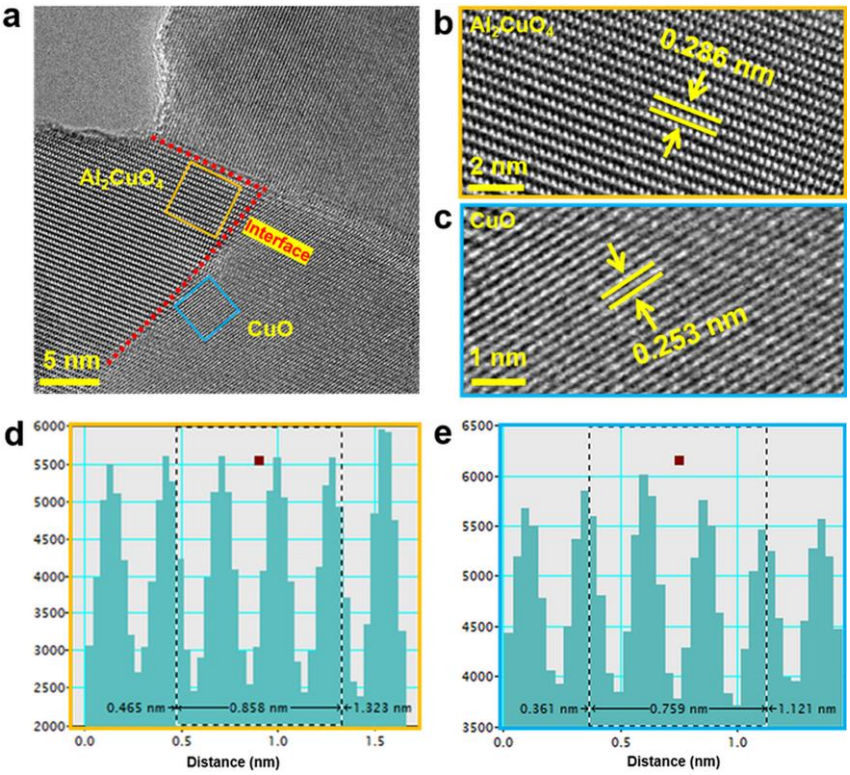

Fig. S1. (a) HR-TEM image of the CuO/Al_2CuO_4 interface in CuAl-**1**. The red dash line marks the interface region between CuO and Al_2CuO_4. (b, d) Magnified HR-TEM image and line intensity profile which is taken from the orange square of Fig. (a). The line intensity profile image in Fig. (d) shows d-spacing values of 0.286 nm, corresponding to the [220] plane of cubic Al_2CuO_4 crystal. (c, e) Magnified HR-TEM image and line intensity profile which is taken from the blue square of Fig. (a). The line intensity profile image in Fig. (e) shows d-spacing values of 0.253 nm, corresponding to the [111] plane of monoclinic CuO crystal.

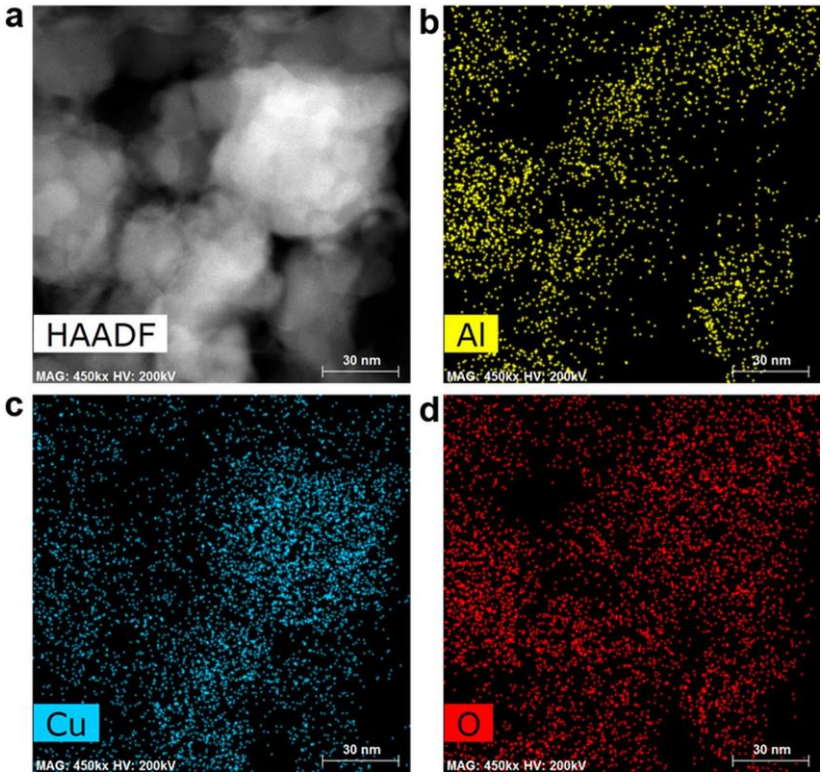

Fig. S2. (a) HAADF-STEM image (used for the atomically resolved high angular annular dark field-scanning transmission electron microscopy-high angle annular dark field (HAADF-STEM) analysis) and (b-d) their corresponding EDS maps of Cu, Al and O. The element maps suggest two types of morphology in CuAl-**1**; **a** mixture of Cu, Al and O in the nanosheet and Cu and O in the nanoparticles.

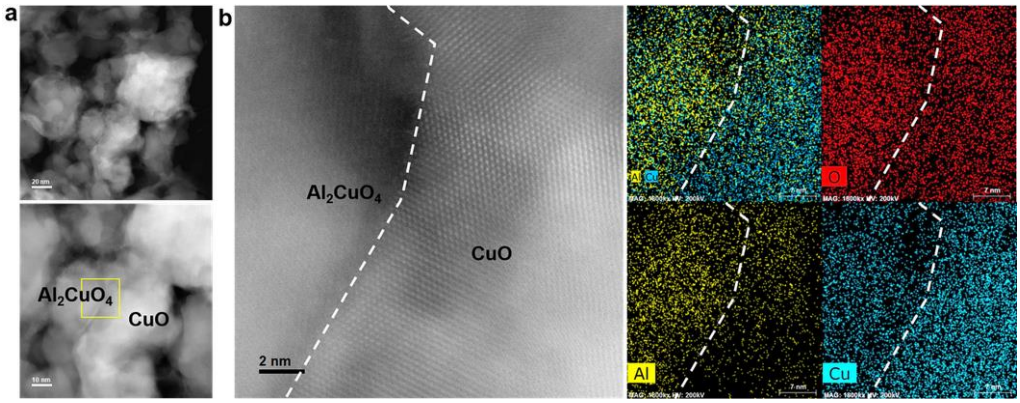

Fig. S3. (a) Low-magnification of HAADF-STEM image (b) The atomic resolution STEM image of the of CuO/Al_2CuO_4 interface (left) and the corresponding overlay map of Cu/Al as well as individual element maps of Cu, Al and O (right) taken from the orange square of Fig. a (bottom). The white dash line in STEM image of fig. b (left) and element maps (right) clearly show the interface structure between CuO and Al_2CuO_4.

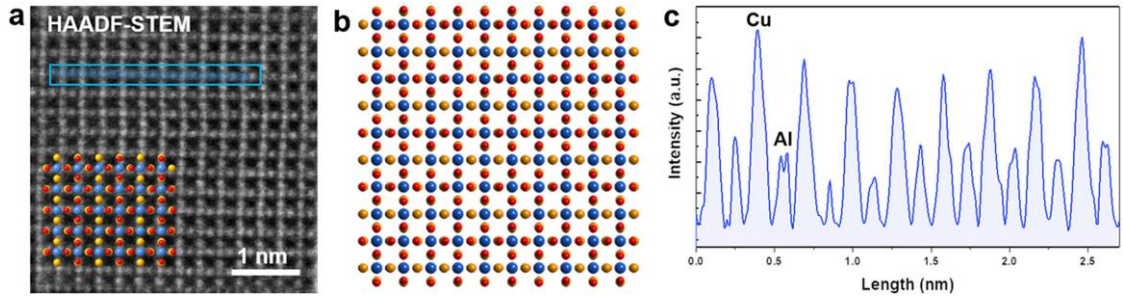

Fig. S4. (a) HAADF-STEM image of Al_2CuO_4 crystal in CuAl-1 viewed along [100] zone direction. The inset structure on the lattice sites are the ball and stick models for the Al_2CuO_4 crystal. (b) Simulated structure model of spinel-type cubic Al_2CuO_4 crystal.[3] The blue, yellow and red balls in the inset and simulated structure models refer, respectively to the atoms of Cu, Al and O. (c) The line intensity profile taken from the atomic column which is marked with a blue line in Fig. (a). The line intensity profile conforms distribution of both Cu and Al elements in each atomic column.

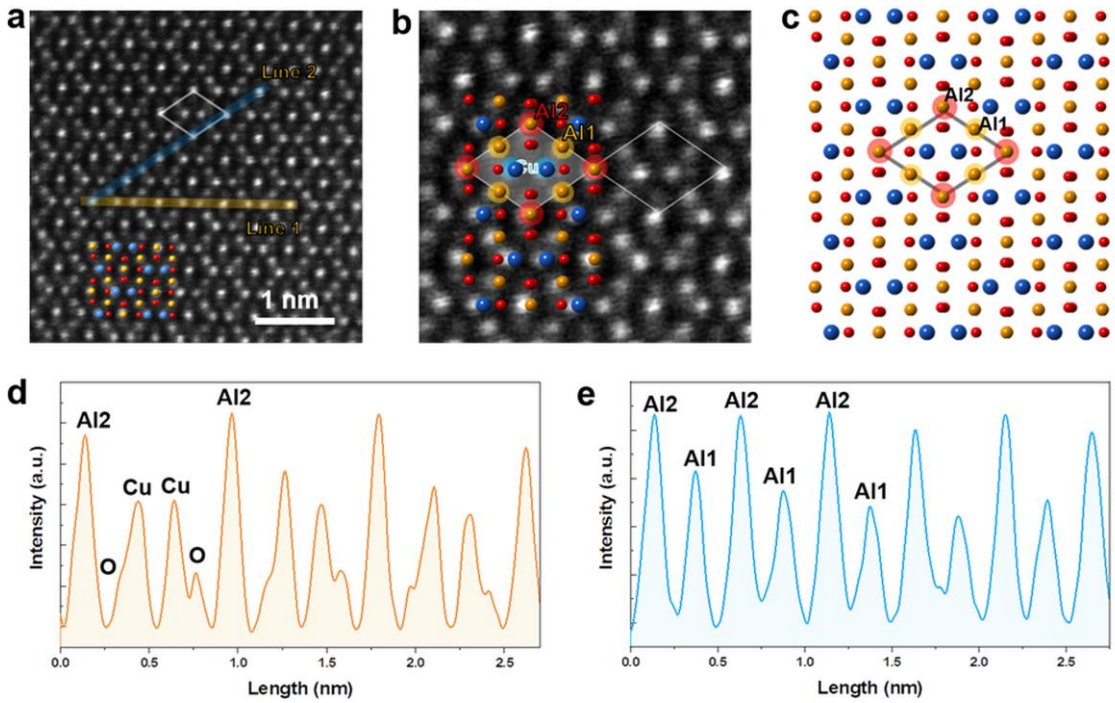

Fig. S5. (a) HAADF-STEM image of Al_2CuO_4 crystal structure in CuAl-**1** viewed along [110] zone direction. (b) Magnified HAADF-STEM image of Al_2CuO_4 taken from Fig. (a). (b) The atomic arrangement of the Al_2CuO_4 coincides with (c) the atomic model of Al_2CuO_4 crystal along with the [110] orientation. In the structure models of Al_2CuO_4 (Fig. c and the inset of Fig. b), we mark the Al on the base of its position in the crystal as Al**1** and Al**2**. (d) The line intensity profile is taken from the atomic column marked with an orange line in Fig. a. (e) The line intensity profile taken from the atomic column marked with a blue line in Fig. S5 (a). The figure denotes that the Al**2** has larger aluminum content in the atomic column than Al**1**. These results are consistent with the previous references,[3] and support that the Al_2CuO_4 in CuAl-**1** has a well-crystallized structure without defects. The blue, yellow and red balls in the inset and structure models refer, respectively to the atoms of Cu, Al and O.

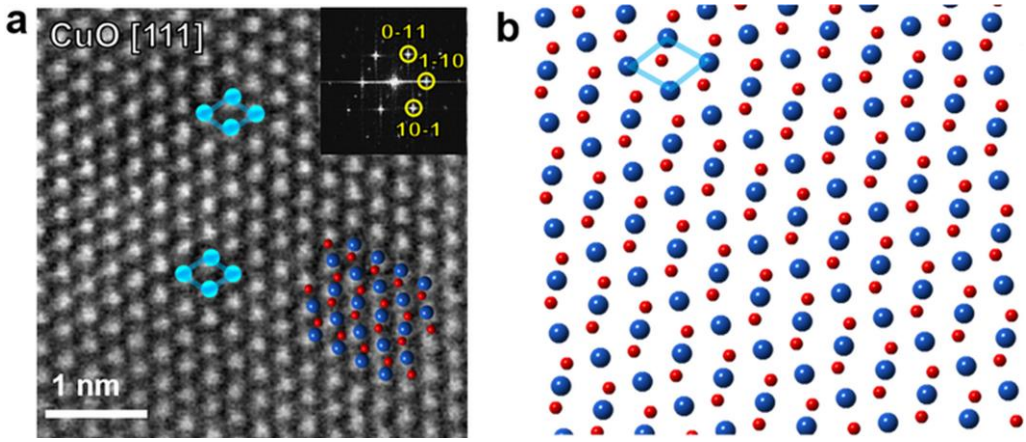

Fig. S6. (a) HAADF-STEM image of CuO crystal in CuAl-**1** viewed along [111] zone direction. The inset structure on the lattice sites are the ball and stick models for the monoclinic CuO crystal. (b) Crystal structure of monoclinic CuO crystal structure. The blue and red balls in the inset and structure models refer, respectively to the atoms of Cu and O.

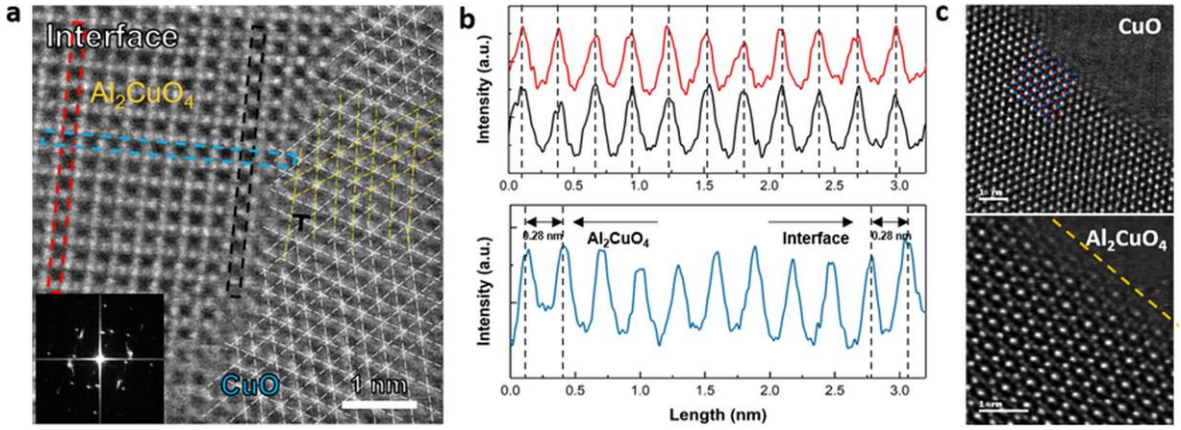

Fig. S7. (a) Atomic-resolution HAADF-STEM image at an interface of CuO and Al_2CuO_4 in CuAl-1. Local lattice distortion of CuO phase induced by adjacent interfacial defects is marked as yellow lines. (b) Line intensity profile for measuring lattice spacing of Al_2CuO_4. Each plot is measured from the marked regions in (a), and it shows that tensile or compressive strain does not exist in the CuO/Al_2CuO_4 interface. (c) HAADF-STEM images of CuO and Al_2CuO_4 do not show any surface reconstruction at the edges.

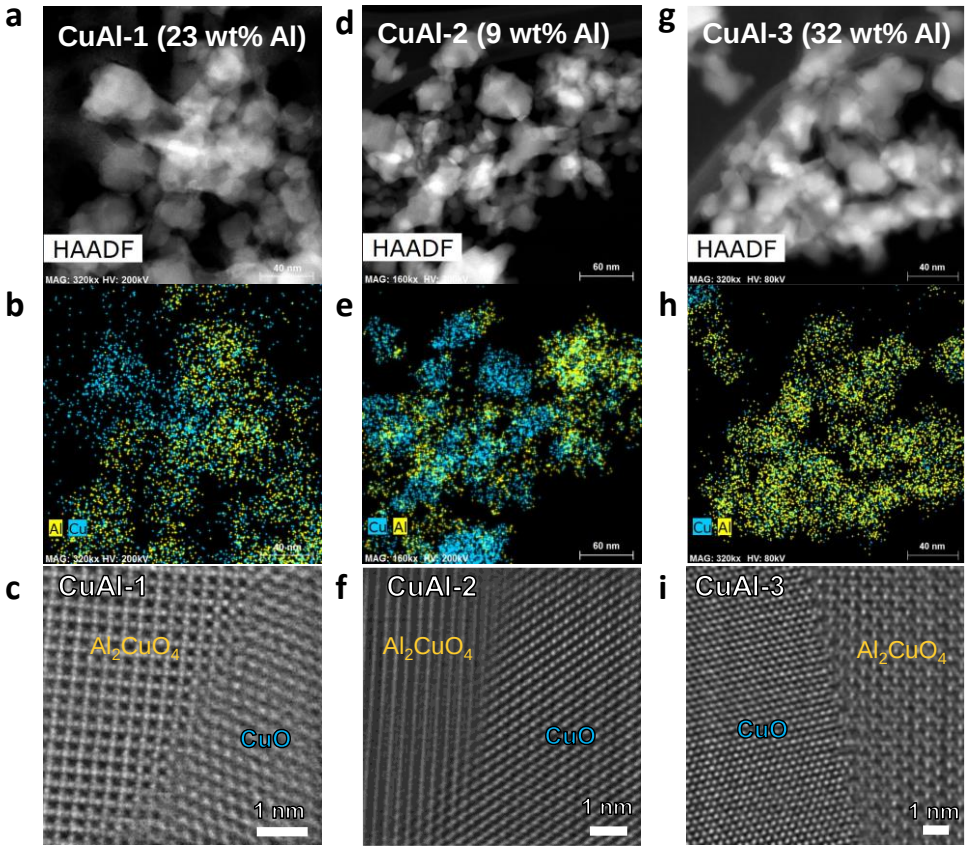

Fig. S8. HAADF-STEM images and their corresponding EDS mapping and atomic-resolution STEM images of CuAl-**1**, CuAl-**2**, CuAl-**3.** (a-c) CuAl-**1** (d-f) CuAl-**2** (g-i) CuAl-**3**.

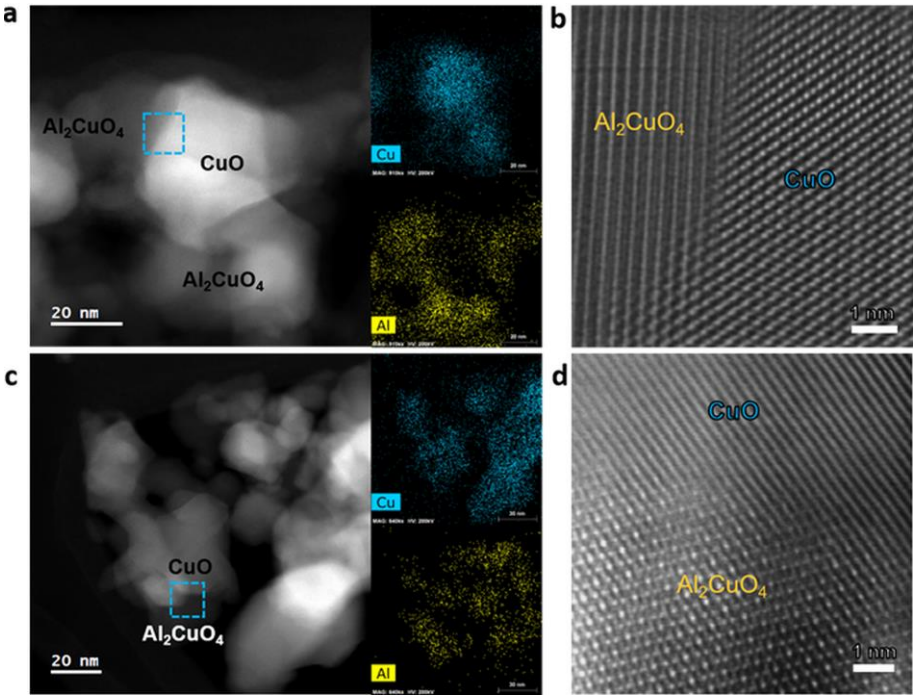

Fig. S9. (a, c) HAADF-STEM images and their corresponding individual element maps of Cu and Al in CuAl-**2**. (b, d) HAADF-STEM images at the CuO/Al_2CuO_4 interface, taken from the region marked in (a, c), respectively.

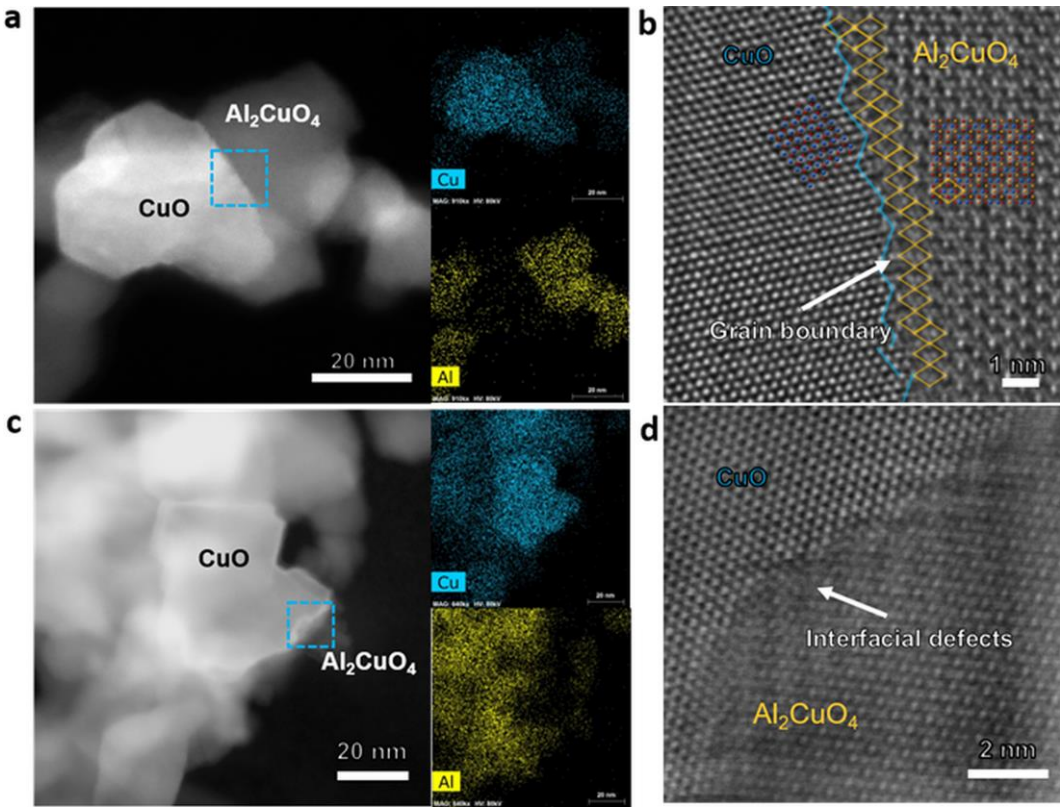

Fig. S10. (a, c) HAADF-STEM images and their corresponding individual element maps of Cu and Al in CuAl-**3**. (b, d) HAADF-STEM images at the CuO/Al_2CuO_4 interface, taken from the region marked in (a, c), respectively.

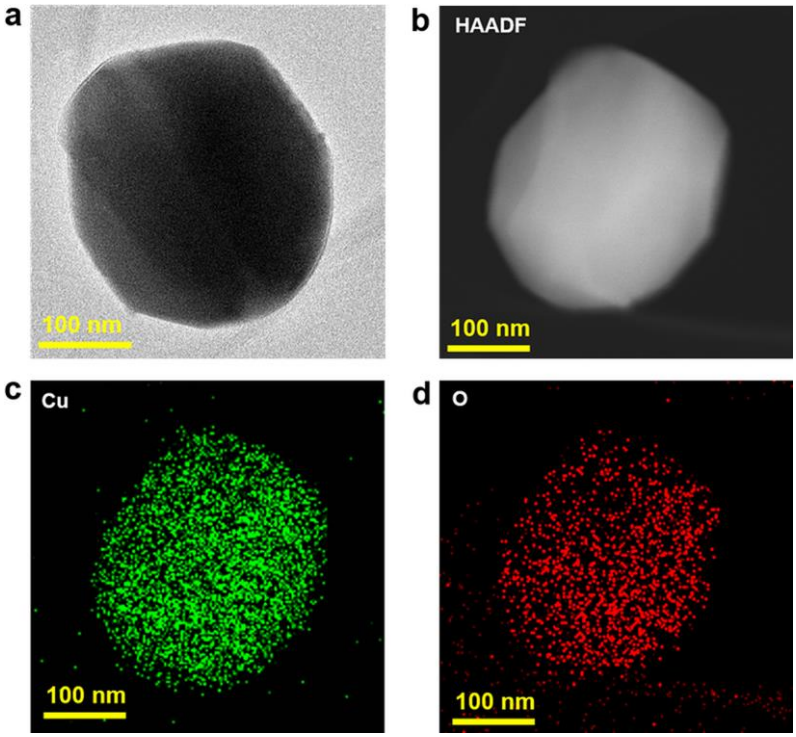

Fig. S11. Morphology characterization of CuO. (a) TEM image (b) HAADF–STEM image and (c and d) corresponding individual element maps of Cu and O.

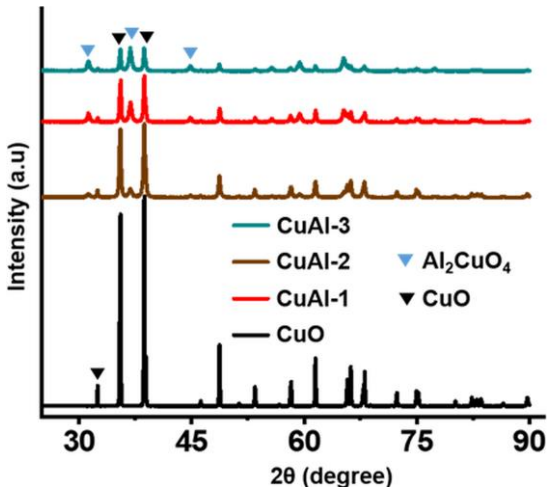

Fig. S12. XRD spectra for CuO, CuAl-**1**, CuAl-**2** and CuAl-**3** catalysts: The XRD pattern of CuO catalyst shows the diffraction peaks at position 2Θ of 32.52°, 35.49°, 38.689°, 48.66°, 58.25°, 61.52°, 66.15°, and 68.88°, corresponding respectively (110), (-111), (111), (-202), (202), (-113), (-311) and (220) planes of monoclinic CuO crystal structure (JCPDS# 01-080-1916). In XRD patterns of CuAl-**1** to CuAl-**3** catalysts, the peaks related to the monoclinic Cu crystal structure weakened in favor of new diffraction peaks at 31.26°, 36.86°, 44.79°, and 55.62° that can be assigned respectively to (220), (311), (400) and (422) lattices of Al_2CuO_4 (JCPDS# 01-076-2295). The new evolved peaks grew in intensity with increasing the amount of Al in the catalysts.

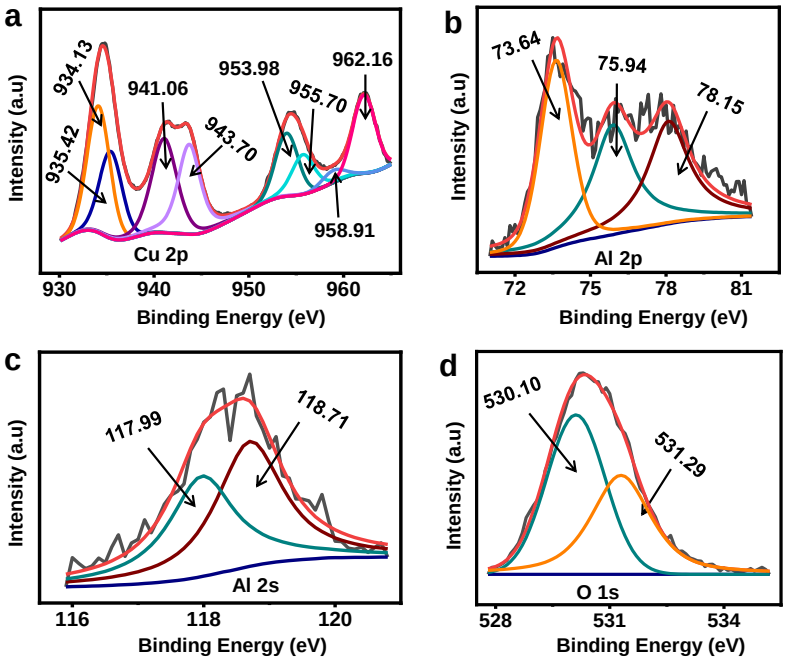

Fig. S13. XPS core-level spectra of CuAl-**1** (a) Cu 2p (b) Al 2p (c) Al 2s (d) O 1s.

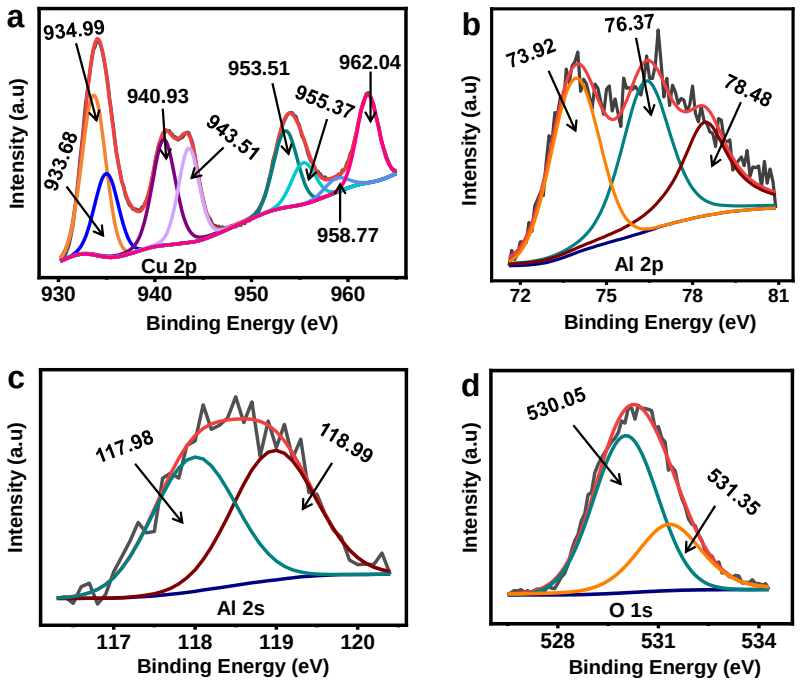

Fig. S14. XPS core-level spectra of CuAl-2 (a) Cu 2p (b) Al 2p (c) Al 2s (d) O 1s.

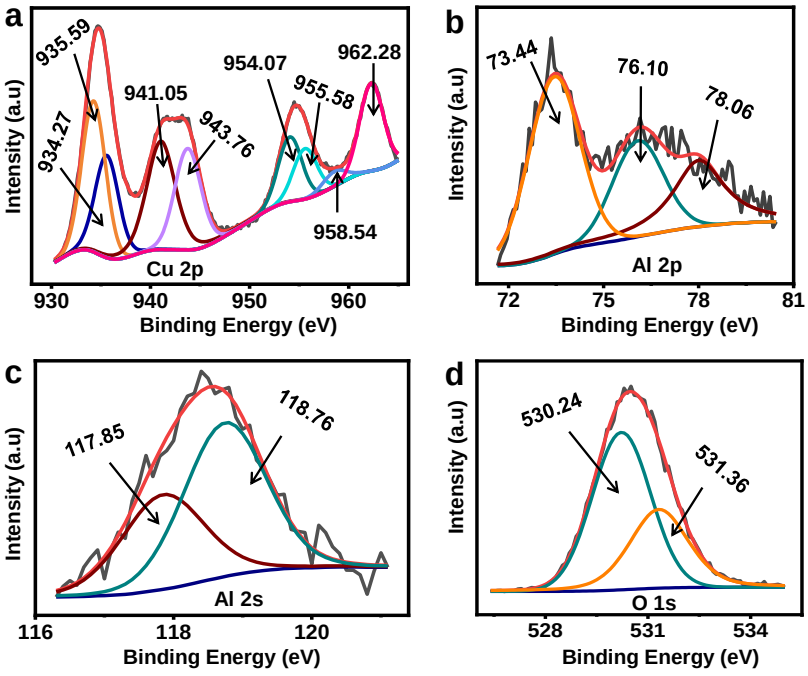

Fig. S15. XPS core-level spectra of CuAl-3 (a) Cu 2p (b) Al 2p (c) Al 2s (d) O 1s.

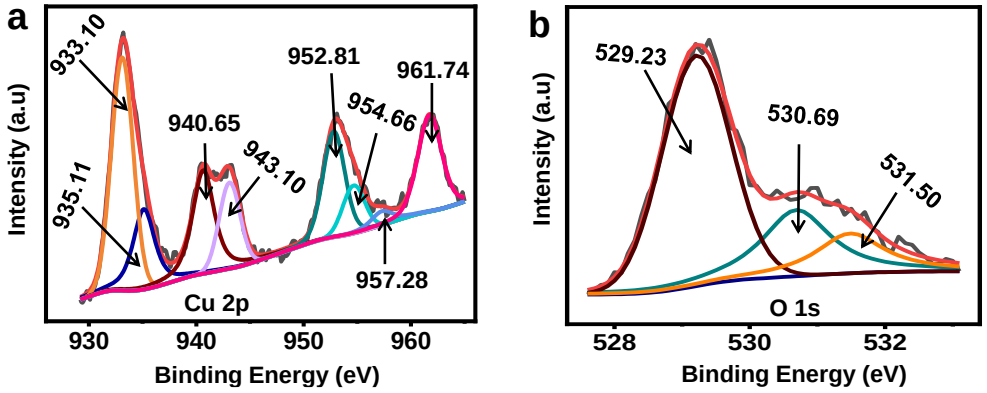

Fig S16. XPS core-level spectra of CuO (a) Cu 2p (b) O 1s. The O-1s XPS spectrum shows two peaks of metal oxide species at 530.69 and 531.50 eV and one peak of the lattice oxygen at 529.23 eV.[4]

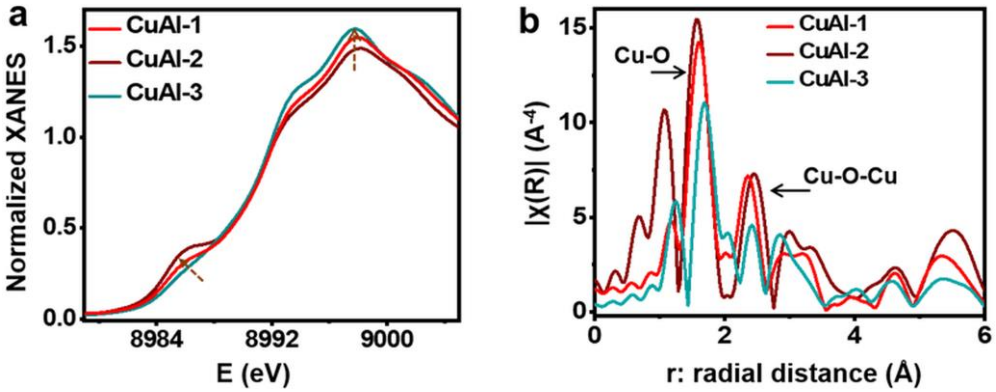

Fig. S17. X-ray absorption spectra CuAl-**1**, CuAl-**2** and CuAl-**3** catalysts. (a) XANES spectra in real space at Cu K-edges. The Cu K-edges from CuAl-**1** to CuAl-**3** gradually shifts to the high-energy direction and the white-line peak intensity increases from CuAl-**1** to CuAl-**3**, suggesting that the average oxidation state of Cu increased with the increase of Al amount from CuAl-**1** to CuAl-**3**. (b) FT–EXAFS spectra in r-space. The FT–EXAFS spectra are consistent with the XANES data.

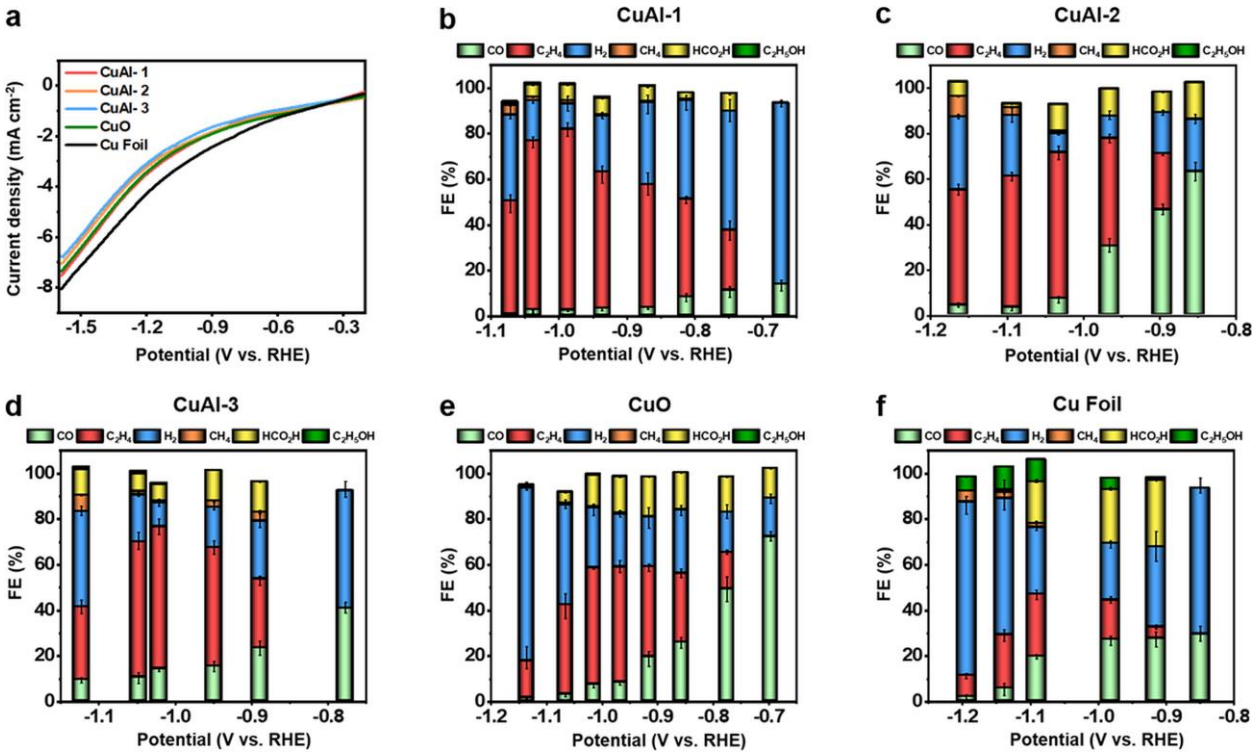

Fig. S18. Linear sweep voltammograms (LSVs) curves and overall gas and liquid products during the electrocatalytic CO_2RR of CuAl-**1**, CuAl-**2**, CuAl-**3**, CuO and electropolished polycrystalline Cu foil in an H-cell. (a) LSV curves in CO_2 saturated 0.1 M $KHCO_3$ electrolyte. (b-f) Product distributions (CO, C_2H_4, H_2, CH_4, HCO_2H and C_2H_5OH) and corresponding Faradaic efficiencies produced by (b) CuAl-**1** (c) CuAl-**2** (d) CuAl-**3** (e) CuO and (f) electropolished polycrystalline Cu foil at different applied potentials in CO_2 saturated 0.1 M $KHCO_3$ electrolyte.

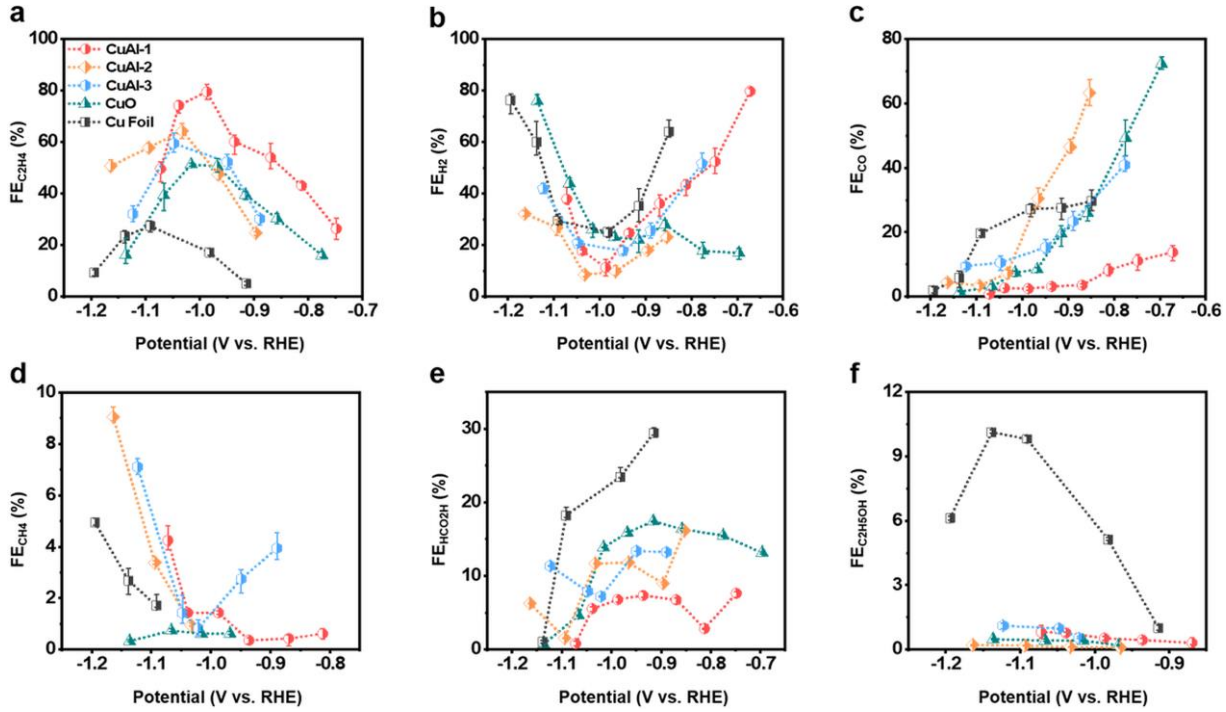

Fig. S19. Comparison of Faradaic efficiencies for different gaseous and liquid products on CuAl-**1**, CuAl-**2**, CuAl-**3**, CuO and electropolished polycrystalline Cu foil in an H-cell. (a) C_2H_4 Faradaic efficiencies (b) H_2 Faradaic efficiencies (c) Co Faradaic efficiencies (d) CH_4 Faradaic efficiencies (e) HCO_2H Faradaic efficiencies (f) C_2H_5OH Faradaic efficiencies.

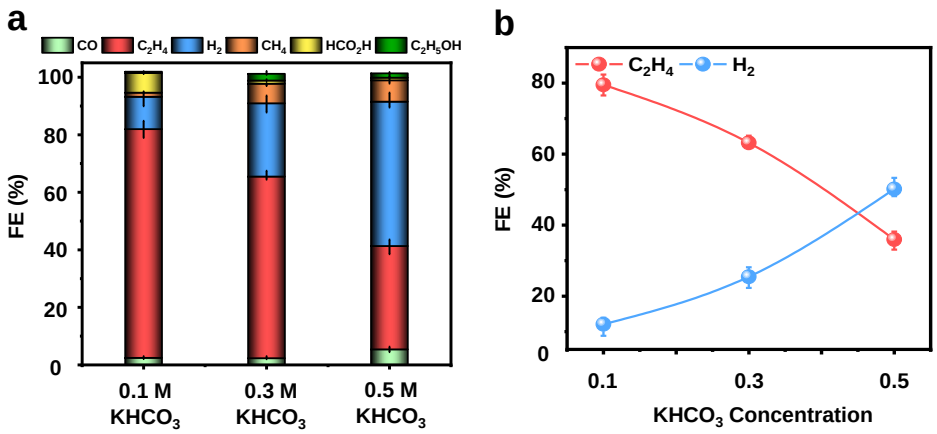

Fig. S20. Electrocatalytic CO_2RR of CuAl-**1** in H-cell with CO_2 saturated with different concentrations of CO_2 saturated $KHCO_3$ electrolytes. (a)Product distributions (CO, C_2H_4, H_2, CH_4, HCO_2H and C_2H_5OH) and corresponding Faradaic efficiencies (b) C_2H_4 and H_2 Faradaic efficiencies along with the concentration of $KHCO_3$ electrolyte. The CO_2RR on CuAl-1 in the H-cell under the different $KHCO_3$ concentrations indicate that CO_2RR to C_2H_4 is more favorable in a dilute $KHCO_3$ solution. However, under a high $KHCO_3$ concentration, the production of H_2 and CH_4 was promoted and ethylene was suppressed. Electrolytes with high buffer capacity such as concentrated $KHCO_3$ solution with high proton concentrations allowed coupled electron/proton transfer and therefore promotes the higher yield of H_2 and CH_4 production. On the other hand, electrolytes with low buffer capacity such as diluted $KHCO_3$ solution make the formation of H_2 and CH_4 less favorable due to a low proton concentration near the surface and increased the formation of C_{2+} product. Also, in concentrated $KHCO_3$ solution, a large amount of K^+ ions are attached near the cathode due to its positive electric property which blocks the access of the CO_2 molecule to the cathode surface and suppresses the CO_2RR.

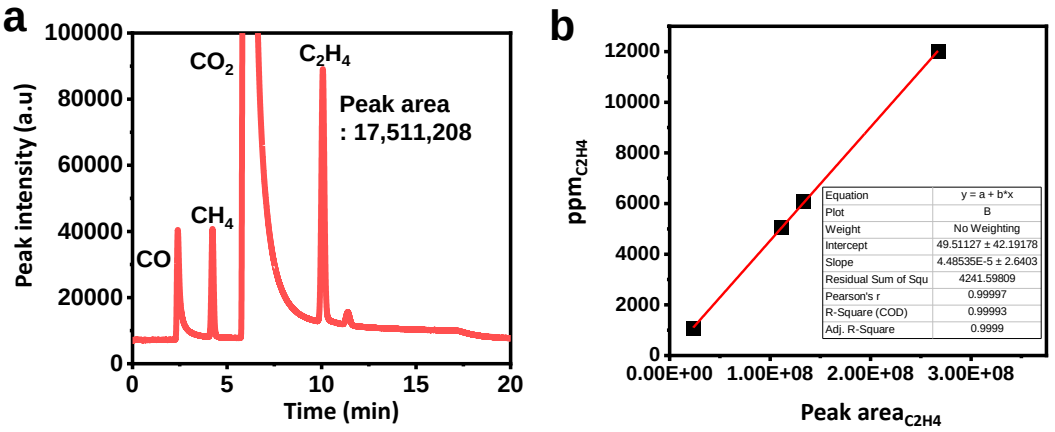

Fig. S21. (a) Raw GC Flame ionization detector data of CO_2RR for CuAl-1 in H-cell with CO_2 saturated 0.1 M $KHCO_3$ electrolyte at -0.99 V_{RHE} (b) GC calibration data of C_2H_4.

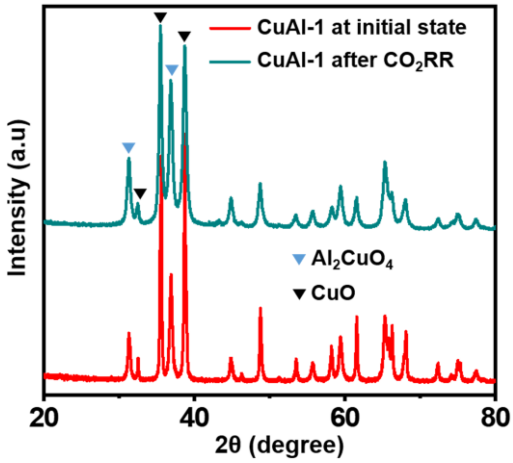

Fig. S22. Comparison of XRD spectra of CuAl-**1** before and after CO_2RR stability test. The position of the peaks for CuAl-**1** before and after the CO_2RR stability test remains almost the same.

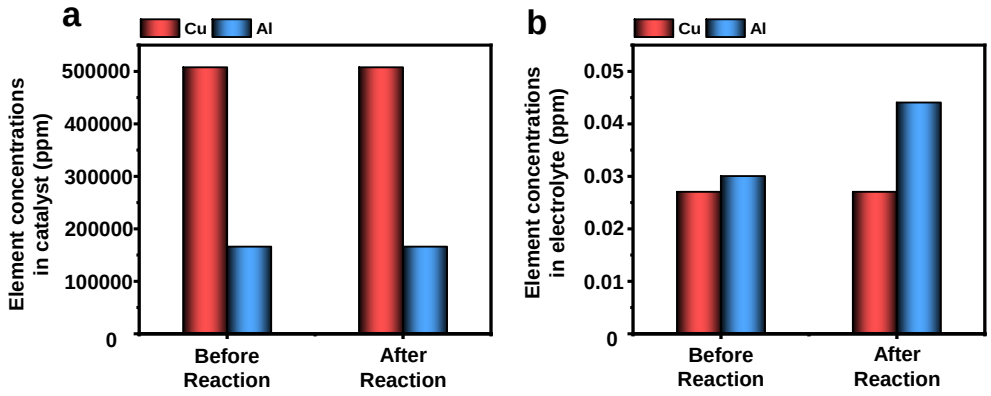

Fig. S23. ICP–OES analysis of the CuAl-**1** before and after the CO_2RR stability test. (a) The concentration of Cu and Al (ppm) in CuAl-**1** before and after the stability test. The terms before reaction and after reaction in Fig. (a) refer to the catalyst in the initial state and after the long-term stability test. (b) The concentration of Cu and Al (ppm) in working electrolyte before and after stability test. The terms before reaction and after reaction in Fig. (a) refer to electrolytes before the applied potential and after the long-term stability test. According to ICP–OES analysis data, the Cu and Al do not leach into the solution, which indicates that the Cu/Al components in the CuAl-**1** catalyst were well preserved during the long-term CO_2RR stability test.

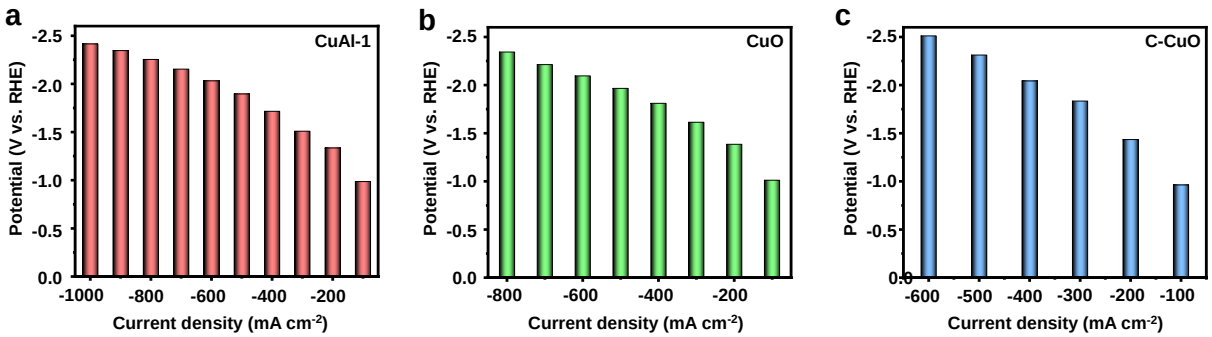

Fig. S24. The overpotential values versus RHE at applied current densities (100-1000 mA cm^{-2}) via chronopotentiometry test for the electrochemical CO_2RR on CuAl-**1**, as-synthesized CuO and commercial CuO in flow cells with CO_2 saturated 1 M KOH electrolyte. (a) CuAl-**1** (b) as-synthesized CuO and (c) commercial CuO.

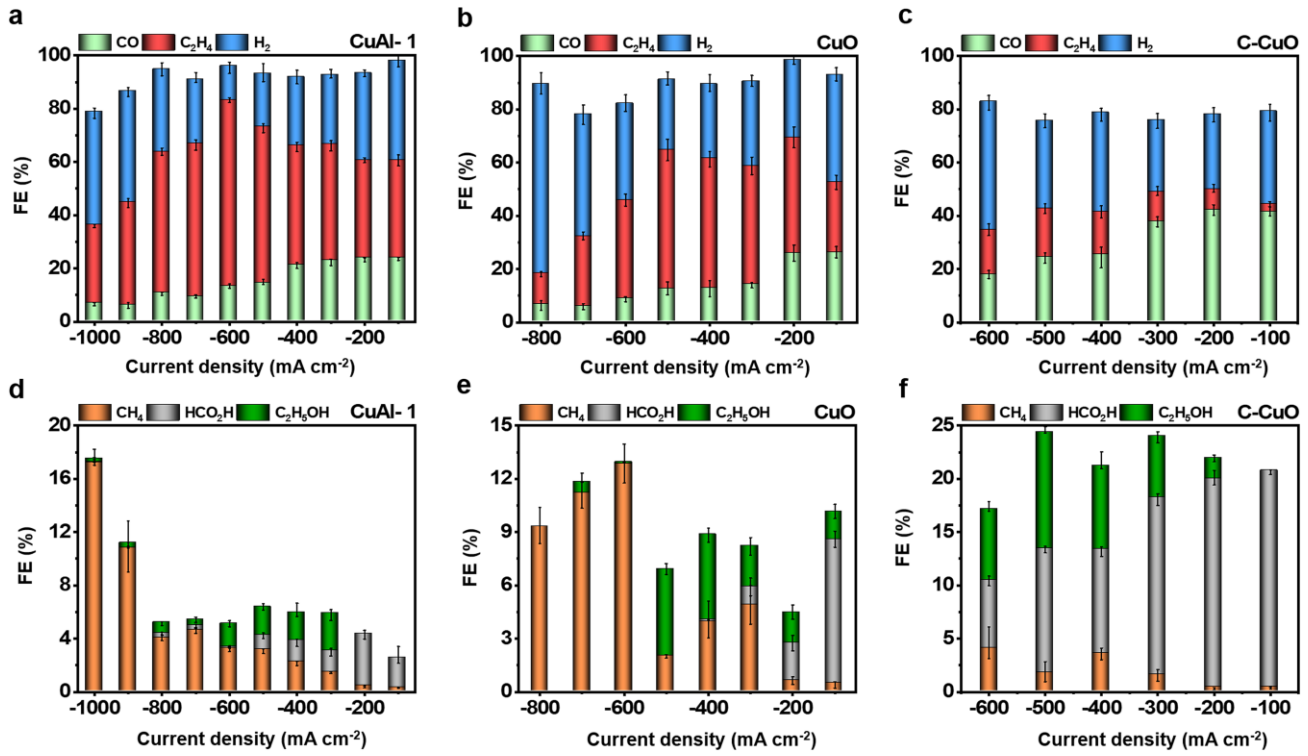

Fig. S25. Electrocatalytic CO_2RR of CuAl-**1**, as-synthesized CuO and commercial CuO in flow cells with CO_2 saturated 1 M KOH electrolyte. (a-c) Co, C_2H_4 and H_2 product distributions and corresponding Faradaic efficiencies produced by (a) CuAl-**1** (b) as-synthesized CuO and (c) commercial CuO. (d-f) CH_4, HCO_2H and C_2H_5OH product distributions and corresponding Faradaic efficiencies produced by (d) CuAl-**1** (e) as-synthesized CuO and (f) commercial CuO.

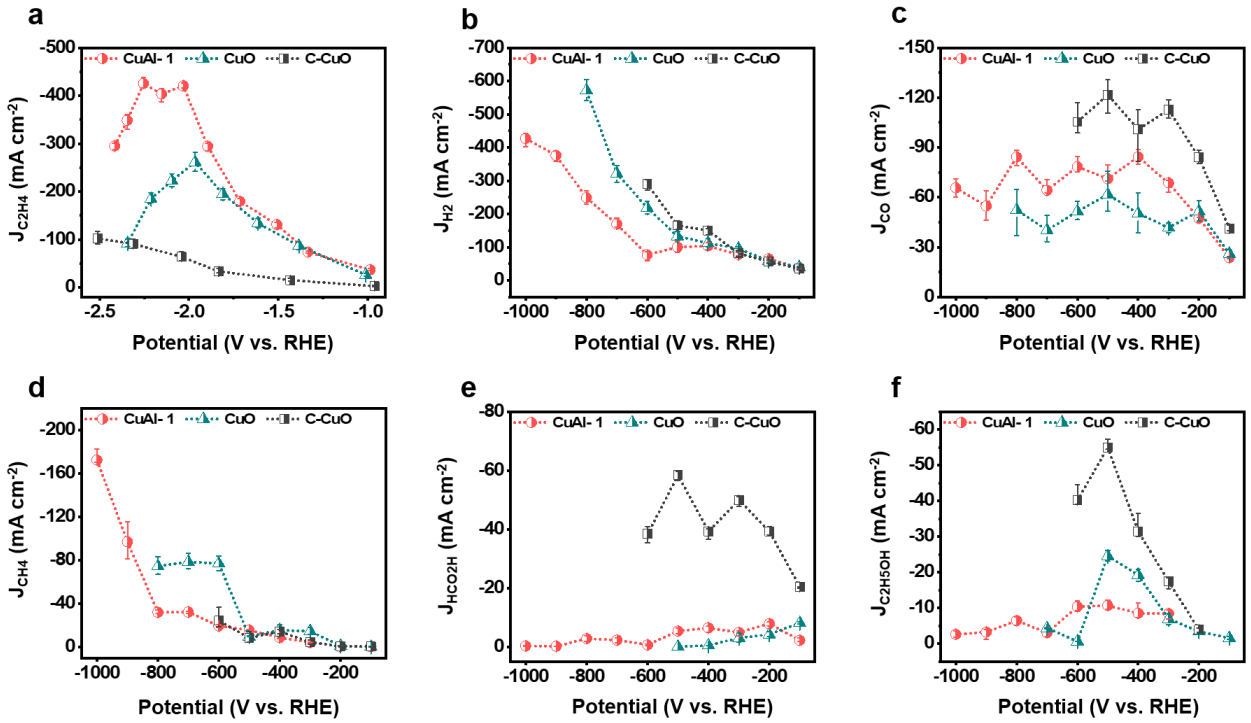

Fig. S26. Comparison of Partial current density for different gaseous and liquid products on CuAl-**1**, as-synthesized CuO and commercial CuO in flow cells with CO_2 saturated 1 M KOH electrolyte. (a) Partial current density of C_2H_4 (b) Partial current density of H_2 (c) Partial current density of Co (d) Partial current density of CH_4 (e) Partial current density of HCO_2H (f) Partial current density of C_2H_5OH.

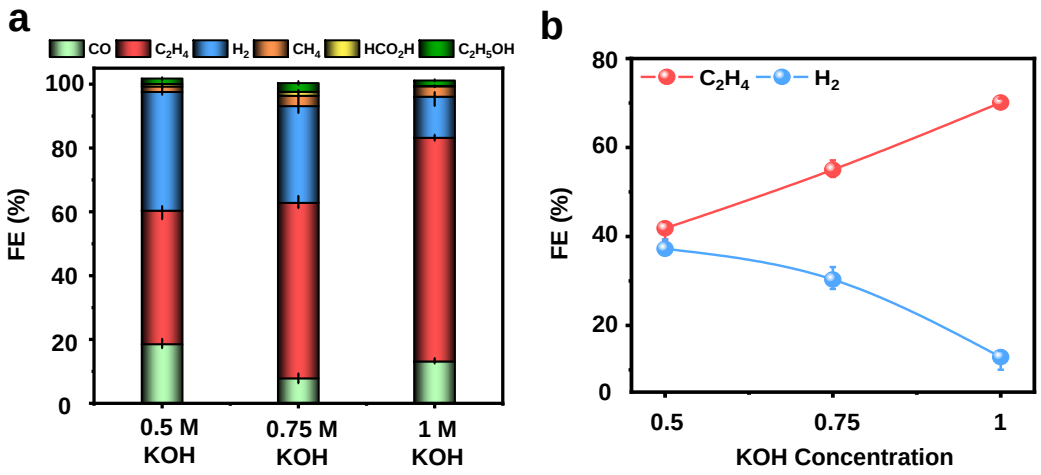

Fig. S27. Electrocatalytic CO_2RR of CuAl-**1** in the flow cells with different concentrations of CO_2 saturated KOH electrolytes at 600 $mAcm^{-2}$ (a) Product distributions (CO, C_2H_4, H_2, CH_4, HCO_2H and C_2H_5OH) and corresponding Faradaic efficiencies (b) C_2H_4 and H_2 Faradaic efficiencies along with the concentration of KOH electrolyte. The CO_2RR on CuAl-1 in the flow cell under the different KOH concentrations indicate that CO_2RR to C_2H_4 is more favorable in a concentred KOH solution. It is ascribed to the fact that the concentrated KOH solution helps in HER suppression during the CO_2RR (HER has sluggish kinetics in a highly alkaline pH) and also the high concentration of OH^- ions reduces the energy barrier for C–C coupling facilitating the formation of C_{2+} product rather than C_1 or H_2 formation.

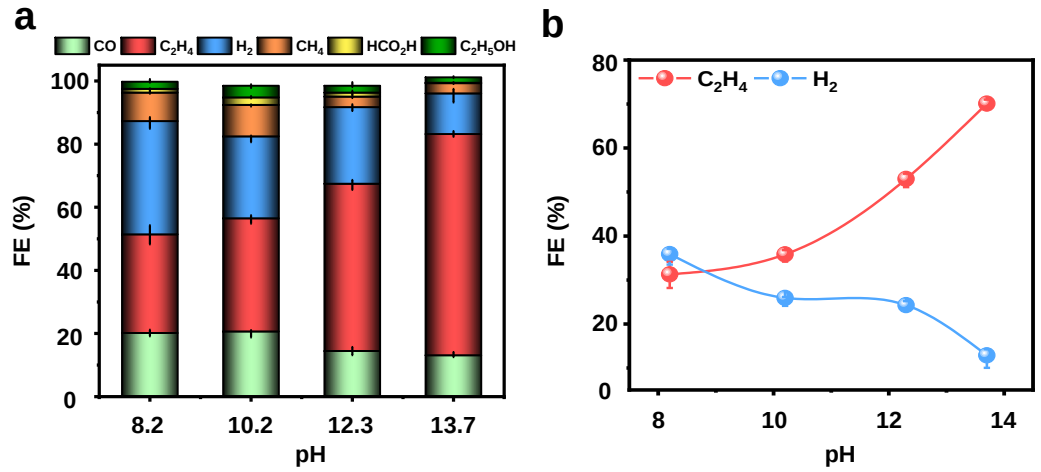

Fig. S28. Electrocatalytic CO_2RR of CuAl-**1** in the flow cells with different pH values at 600 $mAcm^{-2}$. The pH values were adjusted to 8.2, 10.2, 12.3 and 13.7 by mixing the different volumes of 1M $KHCO_3$ and 1M KOH solutions in working electrolyte (a) Product distributions (CO, C_2H_4, H_2, CH_4, HCO_2H and C_2H_5OH) and corresponding Faradaic efficiencies (b) C_2H_4 and H_2 Faradaic efficiencies along with increasing pH.

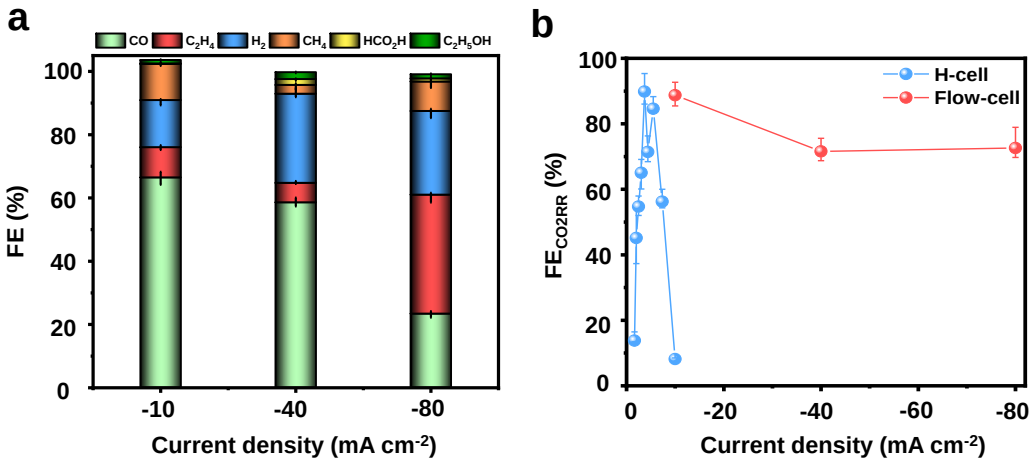

Fig. S29. (a) Electrocatalytic CO2RR of CuAl-**1** in the flow cells with CO_2 saturated 0.1 M $KHCO_3$ electrolyte (b) Comparison of Electrocatalytic CO2RR of CuAl-**1** in H-cell and Flow cell with CO_2 saturated 0.1 M $KHCO_3$ electrolyte. Fig. b shows that HER occurs dominantly at high current density (-10 mA cm-2) in H-cell due to the low mass transfer issue of the CO_2 to the cathode part. On the other hand, the 0.1 M KCO_3 in the flow cell maintained high selectivity toward CO_2RR at the relatively high current densities, however, the flow cell with CO_2 saturated 0.1 M $KHCO_3$ electrolyte cannot achieve a high-density value compared to 1M KOH solution, since the 0.1 M $KHCO_3$ electrolyte requires high overpotential due to its high ohmic resistance/ohmic losses and poor conductivity as well as the poor oxygen evolution reaction performance of anode catalyst in neutral solutions (CO_2RR process pairs two half-reactions of CO_2 reduction and OER. In our study, the NiFeMo alloy was used as an anode).

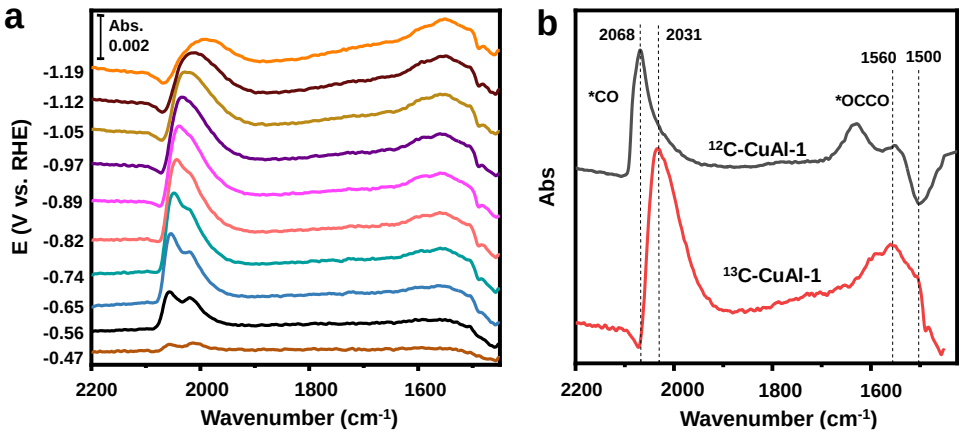

Fig. S30. In situ ATR-SEIRAS analysis for an isotope labelling experiment on CuAl-1. (a) Potential-dependent IR spectra of CuAl-**1** during chronoamperometric scans from -0.47 V to -1.19 V. (b) ^{13}C labelled IR spectrum (red) of CuAl-**1** at -0.97 V in $^{13}CO_2$ saturated 0.1M $KHCO_3$ D_2O electrolyte with baseline spectra at -0.37 V in $^{13}CO_2$ saturated electrolyte. IR spectrum (black) at -0.97 V (^{12}C marked) is also presented as a reference. Experimental condition: $^{13}CO_2$ saturated 0.1M $KHCO_3$ D_2O electrolyte with the baseline spectrum at -0.37 V.

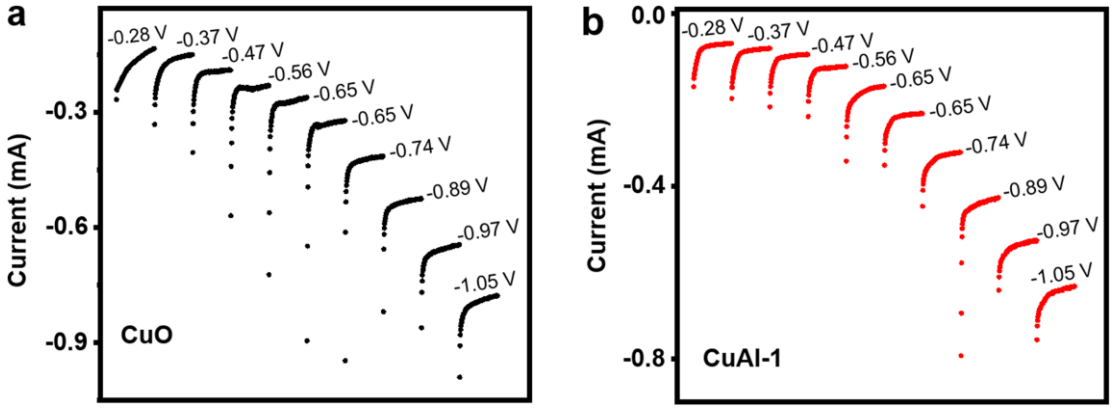

Fig. S31. Chronoamperometric curves of (a) CuO and (b) CuAl-**1** at various individual applied potentials in a CO_2 saturated 0.1 M $KHCO_3$ electrolyte during the ATR-SEIRAS measurement. The potential mention in this figure corresponds to the RHE scale.

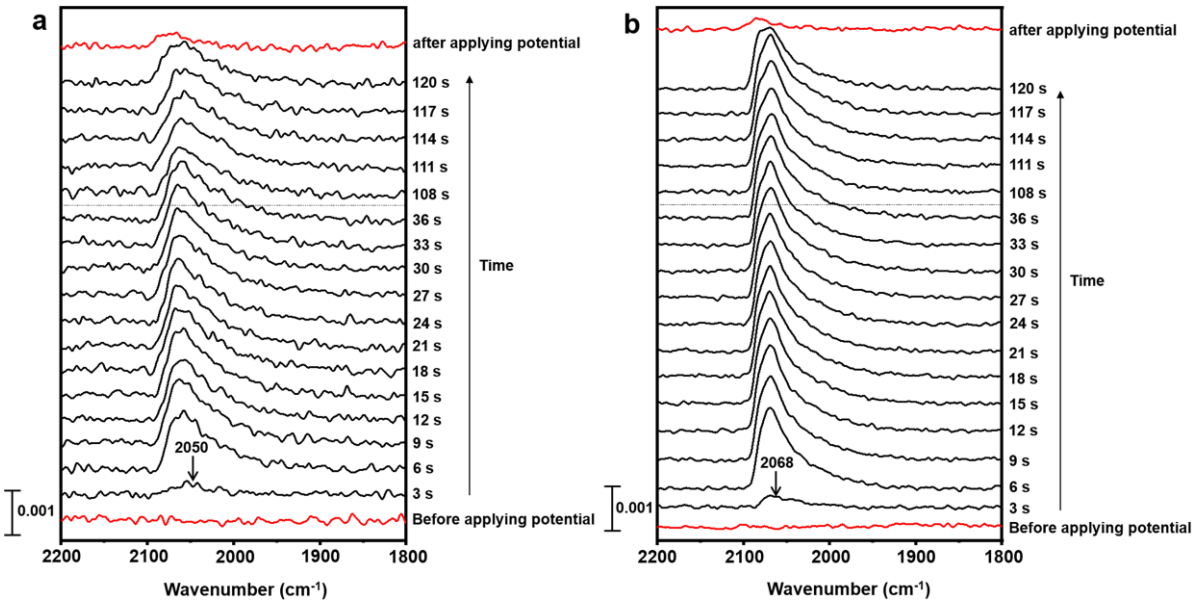

Fig. S32. Time-resolved IR spectra of (a) CuO and (b) CuAl-**1** for an initial 2 min. The spectra were taken in 0.1 M $KHCO_3$ D_2O electrolyte at -0.97 V with the baseline spectra at -0.28 V in CO_2 saturated electrolyte. The potential mention in this figure corresponds to the RHE scale.

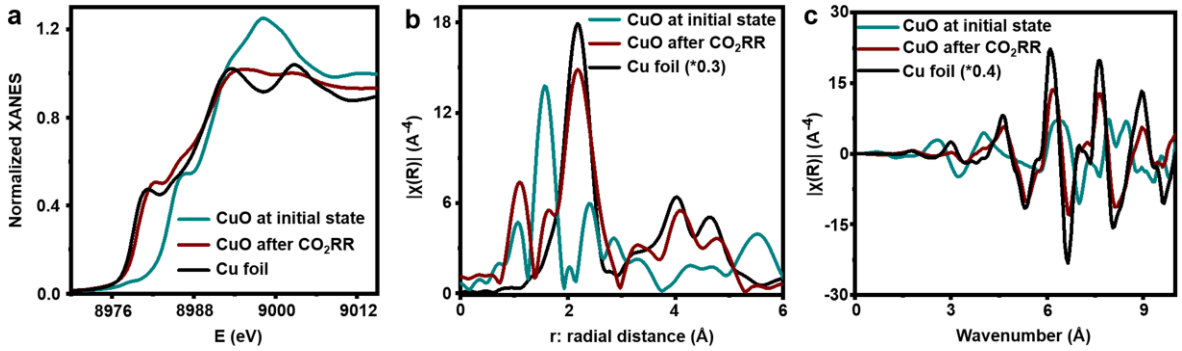

Fig. S33. Comparison of X-ray absorption spectra of CuO catalyst before and after CO_2RR test along with Cu foil reference. (a) XANES spectra in real space at Cu K-edges in CuO. (b) FT–EXAFS spectra in r-space. (c) k3χ oscillation signal in k-space. The Cu K-edge of CuO after the CO_2RR test shows nearly identical pre-edge and white-line peaks the spectrum of a metallic Cu foil. The FT–EXAFS spectra of CuO after the CO_2RR test are consistent with the XANES data; a new strong peak appeared at 2.17 Å, corresponding to the Cu-Cu bonds in metallic Cu. The k3χ oscillation signal of CuO after the CO_2RR test exhibits almost a similar shape in oscillating frequency to the metallic Cu foil.

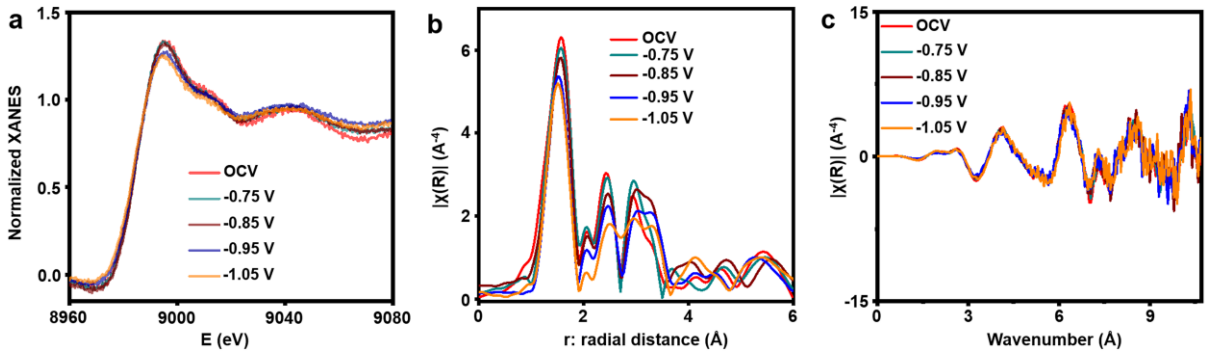

Fig. S34. Operando X-ray absorption analysis to investigate the CuAl-**1** status during the electrochemical CO_2RR at different applied potentials from the open-circuit voltage (OCV) down to -1.05 V in CO_2 saturated 0.1 M $KHCO_3$ solution. (a) XANES spectra in real space at Cu K-edges. (b) FT–EXAFS spectra in r-space. (c) k3χ oscillation signal in k-space. The pre-edge and white-line peaks of Cu K-edge at -0.75 and -0.85 V are almost the same as the spectra of OCV, suggesting that the CuO state in CuAl-**1** remains the same during the CO_2RR. At -0.95 and -1.05 V, the Cu K-edge shifted very slightly toward lower energy and the intensity of white-line peaks was little reduced, indicating that CuO in CuAl-**1** is very slightly reduced during CO_2RR. The FT–EXAFS spectra and k3χ (k) oscillation curves are consistent with the XANES data.

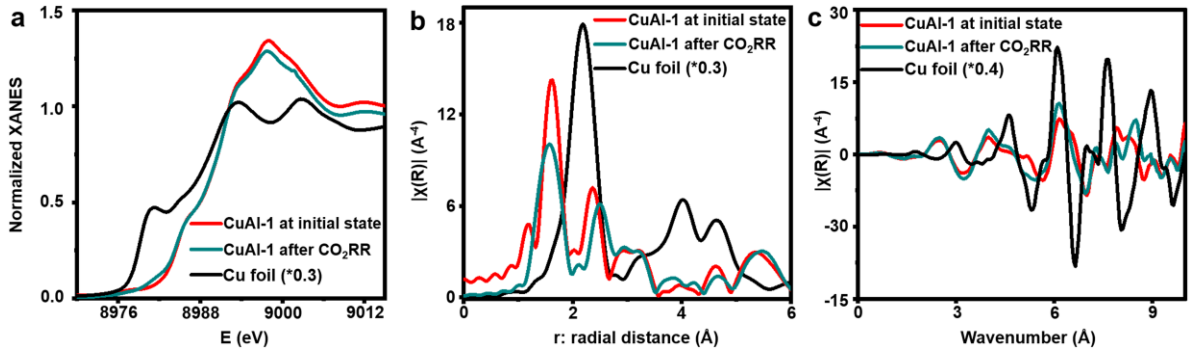

Fig. S35. Comparison of X-ray absorption spectra of CuAl-**1** catalyst before and after CO_2RR test along with Cu foil reference. (a) XANES spectra in real space at Cu K-edges in CuAl-**1**. (b) FT–EXAFS spectra in r-space. (c) k3χ oscillation signal in k-space. The Cu K-edge of CuAl-**1** after the CO_2RR test shows a very small shift towards lower energy compare to pristine CuAl-**1**, indicating that CuO in CuAl-**1** is very slightly reduced during CO_2RR. The radial distance in the FT–EXAFS spectra of CuAl-1 (before and after CO_2RR) are almost the same except for a small shift in the CuO peak towards a lower radial distance after the CO_2RR test. The k3χ (k) oscillation curves of CuAl-**1** after the CO_2RR test show a similar shape in oscillating frequency to that of the pristine electrode and obviously different from that of Cu foil.

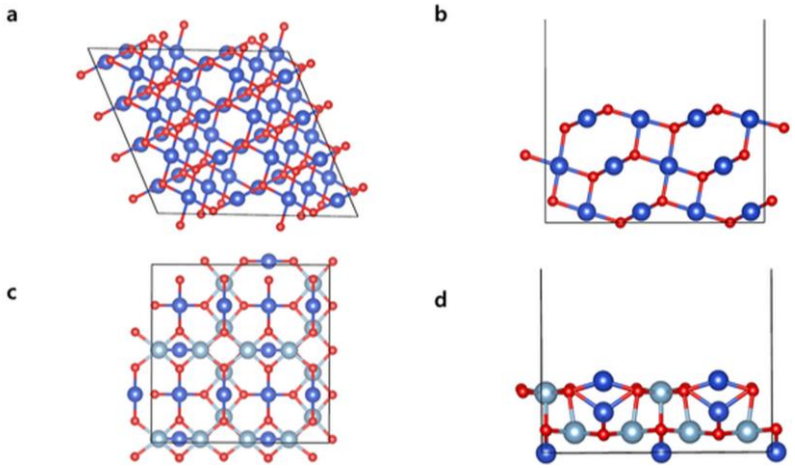

Fig. S36. DFT-optimized structures. (a) Top view and (b) side view of CuO (111) surface slab model. (c) Top view and (d) side view of Al_2CuO_4 (004) surface slab model. Al, Cu, and O are shown as cyan, blue, and red, respectively.

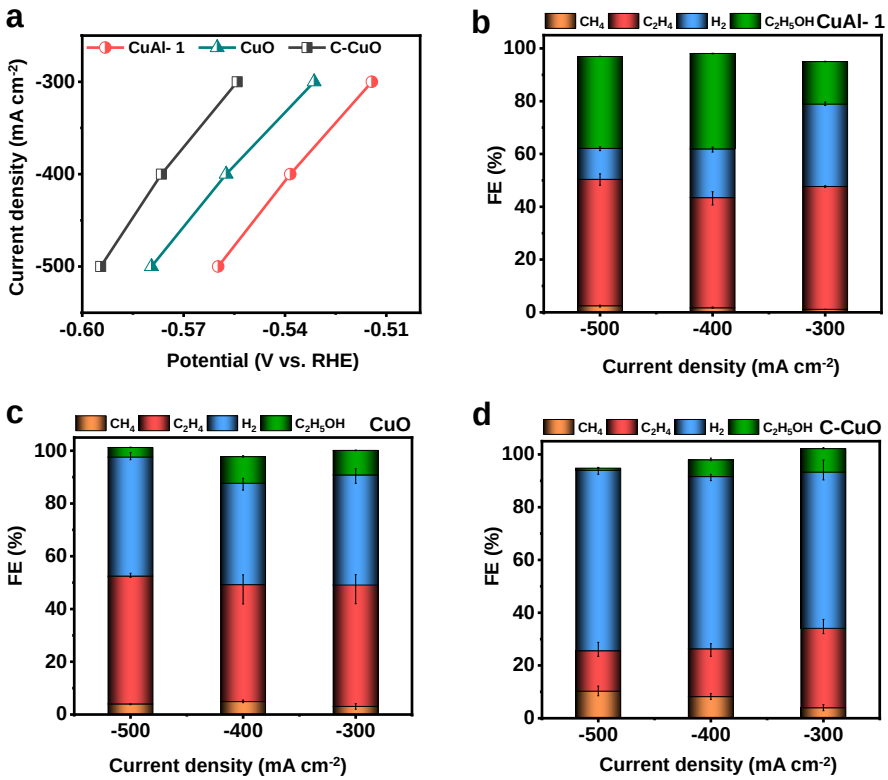

Fig. S37. Electrocatalytic CORR of CuAl-**1**, as-synthesized CuO and commercial CuO in flow cells with CO saturated 1 M KOH electrolyte. (a) The overpotential values versus RHE at applied current densities (300-500 mA cm^{-2}) via chronopotentiometry test for the electrochemical CO_2RR on CuAl-**1**, as-synthesized CuO and commercial CuO (b-d) CH_4, C_2H_4, H_2 C_2H_5OH product distributions and corresponding Faradaic efficiencies produced by (b) CuAl-**1** (c) as-synthesized CuO and (d) commercial CuO.

Table S1. Inductively coupled plasma optical emission spectroscopy (ICP-OES) chemical composition analysis. The ICP-OES analysis of the CuAl-**1** to CuAl-**3** was performed to investigate the wt.% of Cu and Al in each catalyst.

Catalysts	**Cu (wt.%)**	**Al (wt.%)**	**Cu:Al (wt.% ratio)**
CuAl-**1**	51.75	15.54	76.91:23.09
CuAl-**2**	67.00	6.86	90.71:9.29
CuAl-**3**	44.15	20.79	67.99:32.01

Table S2. DFT-calculated surface energies of Al_2CuO_4 for (004) and (220) surfaces, and CO binding free energies on both surfaces.

	Al_2CuO_4 (004)	**Al_2CuO_4 (220)**	**Al_2CuO_4 (111)**
Surface Energy (j/m^2)	1.23	1.47	1.87
*CO Binding Free Energy (eV)	-0.68	-0.34	0.09

Table S3. DFT-calculated hydrogen binding energy, ΔG_H on CuO (111) surface and Al_2CuO_4 (004) surface.

Surface	**ΔG_H (eV)**
CuO (111)	0.63
Al_2CuO_4 (004)	0.97

Table S4. Comparison of electrochemical CO_2RR performances of CuAl-**1** for C_2H_4 with recent reported state-of-the-art Cu-based catalysts in H-cells.

Catalysts	Electrolyte	FE_{C2H4} (%)	Potential (V_{RHE})	Reference
CuAl- I	0.1 M $KHCO_3$	82.40	-0.99	This Work
CuO	0.1 M $KHCO_3$	51.28	-1.02	This Work
Cu Foil	0.1 M $KHCO_3$	27.37	-1.09	This Work
Anodized copper	0.1 M $KHCO_3$	38.1	-1.08	5
Copper(I) oxide films	0.1 M $KHCO_3$	40.00	-0.99	6
Cu NP/C	0.1 M $KHCO_3$	40.50	-1.38	7
Cu Cube	0.1 M $KHCO_3$	41.00	-1.10	8
Cu-I	0.1 M KI	48.00	-0.95	9
Cu(B)-2	0.1 M KCl	52.00	-1.10	10
CuCl-derived catalyst	0.05 M $KHCO_3$	56.00	-1.90	11
Cu_2O NP/C	0.1 M $KHCO_3$	57.3	-1.10	12
Nanostructured oxide layer	0.1 M $KHCO_3$	60.00	-0.90	13
Branched CuO	0.1 M $KHCO_3$	68.00	-1.05	14
Cu nanowire	0.1 M $KHCO_3$	>70.00	-1.00	15

References

1 M. Ma, E. L. Clark, K. T. Therkildsen, S. Dalsgaard, I. Chorkendorff and B. Seger, Energy Environ. Sci., 2020, **13,** 977-985.

2 Y. Kim, S. Park, S.-J. Shin, W. Choi, B. K. Min, H. Kim, W. Kim and Y. J. Hwang, Energy Environ. Sci., 2020, **13**, 4301-4311.

3 L. Li, L. Shi, X. Yu, S. Qing, Z. Gao, Q. Luo, G. Feng and R. Zhang, Chin. Chem. Lett., 2019, 30, 1147-1152.

4 S. Sultan, M. Ha, D. Y. Kim, J. N. Tiwari, C. W. Myung, A. Meena, T. J. Shin, K. H. Chae and K. S. Kim, Nat. Commun., 2019, 10, 5195.

5 S. Y. Lee, H. Jung, N.-K. Kim, H.-S. Oh, B. K. Min and Y. J. Hwang, J. Am. Chem. Soc., 2018, 140, 8681-8689.

6 D. Ren, Y. Deng, A. D. Handoko, C. S. Chen, S. Malkhandi and B. S. Yeo, ACS Catal., 2015, 5, 2814-2821.

7 O. A. Baturina, Q. Lu, M. A. Padilla, L. Xin, W. Li, A. Serov, K. Artyushkova, P. Atanassov, F. Xu, A. Epshteyn, T. Brintlinger, M. Schuette and G. E. Collins, ACS Catal., 2014, 4, 3682-3695.

8 A. Loiudice, P. Lobaccaro, E. A. Kamali, T. Thao, B. H. Huang, J. W. Ager and R. Buonsanti, Angew. Chem. Int. Ed., 2016, 55, 5789-5792.

9 D. Gao, I. Sinev, F. Scholten, R. M. Arán-Ais, N. J. Divins, K. Kvashnina, J. Timoshenko and B. Roldan Cuenya, Angew. Chem. Int. Ed., 2019, 58, 17047-17053.

10 Y. Zhou, F. Che, M. Liu, C. Zou, Z. Liang, P. De Luna, H. Yuan, J. Li, Z. Wang, H. Xie, H. Li, P. Chen, E. Bladt, R. Quintero-Bermudez, T.-K. Sham, S. Bals, J. Hofkens, D. Sinton, G. Chen and E. H. Sargent, Nat. Chem., 2018, 10, 974-980.

11 M. G. Kibria, C.-T. Dinh, A. Seifitokaldani, P. De Luna, T. Burdyny, R. Quintero-Bermudez, M. B. Ross, O. S. Bushuyev, F. P. García de Arquer, P. Yang, D. Sinton and E. H. Sargent, Adv. Mater., 2018, 30, 1804867.

12 H. Jung, S. Y. Lee, C. W. Lee, M. K. Cho, D. H. Won, C. Kim, H.-S. Oh, B. K. Min and Y. J. Hwang, J. Am. Chem. Soc., 2019, 141, 4624-4633.

13 H. Mistry, A. S. Varela, C. S. Bonifacio, I. Zegkinoglou, I. Sinev, Y.-W. Choi, K. Kisslinger, E. A. Stach, J. C. Yang, P. Strasser and B. R. Cuenya, Nat. Commun., 2016, 7, 12123.

14 J. Kim, W. Choi, J. W. Park, C. Kim, M. Kim and H. Song, J. Am. Chem. Soc., 2019, 141, 6986-6994.

15 C. Choi, S. Kwon, T. Cheng, M. Xu, P. Tieu, C. Lee, J. Cai, H. M. Lee, X. Pan, X. Duan, W. A. Goddard and Y. Huang, Nat. Catal., 2020, **3**, 804-812.